Interactional aerodynamics and acoustics of a rotor with an airframe in hover

Si Jin Kim (김시진), Yu-Hyeon Hwang (황유현), Rho Shin Myong (명노신), Hakjin Lee (이학진)*

School of Mechanical and Aerospace Engineering, Gyeongsang National University, Jinju, Gyeongnam 52828, South Korea

*Author to whom correspondence should be addressed: hlee@gnu.ac.kr

Abstract

The demand for the development of urban air mobility (UAM) powered by electric systems has been steadily rising across private and public sectors. Most UAM flights incorporate a distributed electric propulsion (DEP) system to enhance aircraft safety and reliability, which entails an increase in the number of rotors or propellers. Consequently, aerodynamics and aeroacoustics are significantly influenced by strong interactions between the rotor and the airframe. In this study, we conducted a computational investigation to examine the impact of rotor-airframe interaction on aerodynamic and aeroacoustic characteristics. This examination considered variations in airframe shape and the distance between the rotor and airframe. The aerodynamic analysis was executed using the lattice-Boltzmann method (LBM) simulation, in which acoustic predictions were made using the Ffowcs Williams-Hawkings (FW-H) acoustic analogy with a permeable surface. The airframe consists of two geometries: a cylinder and a cone. Tip vortex breakdown and the transition into the turbulent wake state were captured in both airframes, and a fountain flow was affected by the downwash circulation generated under certain proximity of airframe cases. The acoustic prediction results showed that high-intensity noise radiated over the broad surface of the airframe in the conical airframe case. Significant thrust force fluctuations and an increase in noise level were observed at the smallest rotor tip clearance, $S/R = -0.1$, compared to the isolated rotor. Furthermore, the noise contribution of the rotor and airframe was compared, revealing that the airframe noise level was even higher than the rotor noise at $S/R = -0.1$.

1. INTRODUCTION

The demand for a novel transportation system featuring vertical take-off and landing (VTOL) capabilities, low-noise performance, and environmentally friendly power sources, commonly referred to as urban air mobility (UAM) or advanced air mobility (AAM), has experienced a significant surge, especially for public purposes such as medical emergency services and deliveries. With rapid technological progress and heightened global competition, UAM has emerged as an effective solution to alleviate population density and traffic congestion in urban areas. Projections indicate that the global UAM market is poised to reach a staggering $1.5 trillion by 2040[1]. However, it is crucial to proactively address potential risks related to safety, noise, security, and environmental impacts for the successful integration of UAM as a new transportation system. Among these concerns, noise holds a pivotal role, followed closely by safety issues, given the unique operational characteristics of UAM, which often involve flying at low altitudes within densely populated urban areas[2]. The noise disruptions stemming from UAM operations have direct consequences on passengers and nearby residents. An increase in noise pollution-related complaints could potentially hinder public acceptance of this innovative mode of transportation. Therefore, designing low-noise aircraft or developing noise-reduction technologies is crucial for the growth of the UAM industry.

UAM aircraft can be categorized into two main types based on the presence of wings: those with wings (employing lift, cruise, and vectored thrust) and those without wings (using a multicopter design). While the propulsion configurations of UAM aircraft may vary, they commonly feature distributed electric propulsion (DEP) systems with multiple lifting- or prop-rotors. DEP systems offer the advantage of not requiring additional control surfaces since each propulsion unit can be independently controlled. This actuator redundancy, combined with electric propulsion, contributes to enhanced flight stability, maneuverability, and safety. Moreover, DEP systems not only deliver exceptional aerodynamic and propulsion efficiency but also effectively reduce noise emissions. However, the incorporation of multiple propulsion systems inevitably gives rise to rotor-rotor, rotor-fuselage, and rotor-airframe interference phenomena. These interactions can significantly differ from the performance of typical rotary-wing aircraft such as helicopters. Consequently, it is expected that the noise characteristics of a UAM aircraft employing a DEP system will not be qualitatively similar to the noise produced by traditional rotorcraft due to the mutual interactional effects[3-5].

Previous studies have reported that multiple-rotor systems powered by electric propulsion experience significant rotor-to-rotor interactions. Lee and Lee[6] examined the rotor-rotor interactional effects on the rotor

aerodynamics and acoustics of multirotor unmanned aerial vehicle (UAV) in hover flight conditions. These interactions have a notable impact on the formation of rotor wake structures and result in the creation of an asymmetric strong tip vortex, which, in turn, leads to unsteady aerodynamic loads and increased noise. Zhou *et al.*[7] and Shukla *et al.*[8] conducted experimental investigations on the effects of rotor-rotor interaction, using high-resolution particle image velocimetry (PIV) measurements to study the thrust performance and wake structures of small multicopter unmanned aerial vehicles. Meanwhile, Intaratep *et al.*[9] measured thrust performance and noise in small UAVs, exploring how rotor interaction effects vary depending on the number of rotors. Chae *et al.*[10] conducted an experimental analysis of the impacts of rotor-rotor interactions on wake characteristics for a twin-rotor configuration during axial descent. Lastly, Piccinini *et al.*[11] investigated rotor-rotor aerodynamic interactions in electric VTOLs using the vortex particle method. The results of the numerical simulations showed a reduction in thrust efficiency in the tandem configuration, notably when the propeller disks overlapped completely. Jia and Lee[12,13] examined the interactional effects on the aerodynamically induced noise of a side-by-side hybrid VTOL aircraft and quadrotor UAM aircraft through high-fidelity computational analysis, and Li and Lee[14] focused on predicting broadband noise of multirotor UAM vehicles.

Airframes or arms that support the propellers have interactions with the propellers or rotors, thereby influencing the development of downwash and wake structures. The presence of an airframe induces a partial ground effect, which depends on the rotation angle or the location of the propeller[15]. Additionally, the fountain effect is a consequence of the upwash flow generated by the rotor-airframe interaction and has a notable impact on the mechanism that generates noise[16,17]. Hence, it is crucial to account for aerodynamic interference with the structural components of the aircraft when conducting acoustic analysis on UAM aircraft utilizing a DEP system with numerous propellers. Several prior studies have explored the phenomenon of rotor-airframe interaction using a combination of experimental and computational methods. Caprace *et al.*[18] delved into the wake dynamics of a quadcopter during forward flight and examined the influence of rotor-airframe interaction on thrust performance. Zawodny *et al.*[15] conducted high-quality experiments under controlled conditions to investigate the impact of rotor-airframe interaction on the acoustic characteristics of a small-scale rotary-wing unmanned aircraft system (UAS) in an anechoic chamber at the NASA Langley Research Center. Wachspress *et al.*[19] predicted the aerodynamic noise generated by rotor-airframe interaction using CHARM/PSU-WOPWOP and comprehensive rotorcraft analysis codes. Wang *et al.*[20] performed experiments and computational analyses to compare the aerodynamic and aeroacoustic performance of an UAV based on the airframe's position. Zori and Rajagopalan[21] employed the source term of the momentum equation to investigate the interaction effects of a rotor-aircraft model

in forward flight. Park and Jee[22] numerically investigated interactional aerodynamics of a quadcopter in hover, especially focusing on mutual interaction between rotors and rotor and fuselage with airframes.

Based on the above literature, the major gaps in previous studies can be summarized in three ways. First, reported work on the aeroacoustic analysis of the rotor-airframe configuration is limited to investigating the impact of interactional effects on rotor noise. The acoustic contribution from the aerodynamic loads acting on the airframe caused by the rotor wake flow is still unexplored. To the best of our knowledge, this study represents the first attempt to assess the noise levels produced by the rotor and airframe separately while considering variations in the rotor-to-airframe distance. It addresses the airframe's contribution to the overall noise levels. Moreover, a comparative analysis between permeable and impermeable surface methods was conducted to reveal the dominant noise sources in the rotor-airframe configuration. Second, it is important to note that there have been limited systematic investigations into the aerodynamic and acoustic characteristics of rotors with blunt airframes. Although Zawodny and Boyd[15] have already addressed this matter, they did not extensively cover the detailed flow physics related to the interactional aerodynamics. Our research builds upon the work of Zawodny and Boyd[15], examining the same configurations and conditions. In this study, we conducted extensive computational analysis to investigate the rotor-airframe interactional effects on thrust fluctuation, flow field, wake structure, and noise levels. Third, the mainstream approach still relies on traditional computational fluid dynamics (CFD) methods based on finite volume methods (FVM) for simulating the vortex-dominated flow over rotors. It is worth noting that only a few studies have utilized the lattice-Boltzmann method (LBM), which is derived from the Boltzmann kinetic equation. This approach is distinct from the more commonly used numerical simulation based on the Reynolds-averaged Navier–Stokes (RANS) equations. In this study, LBM was employed to predict the rotor aerodynamics and acoustics, and the results were compared against the experimental data and CFD predictions provided by the work of Zawodny and Boyd[15]. This comparative analysis can provide valuable insights into the predictive capabilities of LBM. In this study, the commercial software PowerFLOW was applied to predict the variations in aerodynamic performance and noise sources depending on the airframe shape and separation distance. The Ffowcs Williams-Hawkings (FW-H) equation with a permeable surface was used to investigate the impact of the rotor-airframe interaction on the aerodynamically induced noise. Moreover, we employed impermeable surfaces on both the rotor blades and airframe to evaluate their noise contributions and assess the influences of acoustic scattering and volume noise sources resulting from rotor-airframe interaction.

2. NUMERICAL METHODS

A. Lattice-Boltzmann Methods (LBM)

Most computational analysis studies, including those mentioned previously, rely on the RANS equation. However, solving the RANS equation is a complex and time-consuming task due to its inclusion of nonlinear terms. Moreover, traditional CFD programs introduce simplifications into the Navier–Stokes equations, making it demanding to obtain precise solutions. Although the RANS method is the mainstream approach for simulating the vortex-dominated flow over rotors, it may yield somewhat inaccurate results in predicting the complex structures of rotor tip vortex and wake flow caused by interactions. In our study, it is important to accurately consider the interference effect between the rotor and airframe. Therefore, we aimed to capture the evolution of wake structure and the interference phenomenon accurately, which induces high turbulence near the rotors and the airframe. However, conventional CFD approaches, including RANS, have suffered from the dissipation error caused by the volume discretization, making rotor wake prediction more challenging. However, the dissipation error is only due to a very small amount of artificial viscosity added to the system to stabilize the LBM simulation[23]. As a result, recent research has increasingly turned to the LBM to assess aerodynamic forces and aeroacoustic noise generated by rotorcraft[24-28]. In contrast to conventional numerical methods that discretize macroscopic continuum equations, the LBM is rooted in microscopic models and mesoscopic kinetic equations[29]. It extends from the lattice gas automata (LGA) model, which employs a discrete lattice and discrete time to describe macroscopic complex flows through a micro-world perspective. By doing so, it overcomes limitations such as the inherent white noise in the LGA model due to the statistical nature of automata and the lack of Galilean invariance[30]. In the LBM, the distribution function defined by the Boltzmann equation characterizes the distribution of particles within a discretized lattice[31]. Physical properties like density and momentum are determined using this distribution function. The governing equations of LBM are algebraic and do not contain the partial differential terms, leading to efficient parallel performance and minimal numerical dissipation errors. Given these attributes, LBMs are particularly well-suited for very large eddy simulations (VLES), whereas RANS simulations are difficult to resolve the range of turbulence scales responsible for broadband noise unless combined with semi-empirical models or statistical approaches[32]. The LBM analysis method can be applied to computational aeroacoustics (CAA) analysis, enabling direct calculations of the sound pressure and can be used in conjunction with the Ffowcs Williams-Hawkings (FW-H) method for evaluating far-field noise. Casalino *et al.*[23] used LBM to predict the noise propagation resulting from electric tilt rotors when operating in urban environments. Romani

and Casalino[33] predicted the unsteady aerodynamic loads on rotor blades, rotor wake development, and BVI noise using LBM and validated their results using experimental data. Shubham[34] examined changes in the flow field around a coaxial rotor used in UAM flight vehicles and aerodynamic noise by applying LBM. As mentioned above, LBM has the capability of handling complex fluid behaviors and geometries in many mesoscopic applications and exhibits good scalability in parallel computing performance. Despite these various advantages, it requires the use of Cartesian grids, leading to a dramatic increase in the number of grid points close to the wall[35], which is a potential disadvantage of the LBM method.

In this study, the D3Q19 model was employed to discretize the lattice-Boltzmann equation in a three-dimensional space, dividing the velocity space into 19 discrete speeds, as depicted in Fig. 1[36].

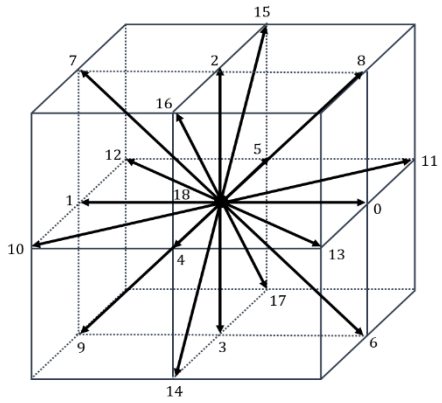

FIG. 1. D3Q19 model for discretizing the lattice-Boltzmann equation

The discrete lattice-Boltzmann equation using a specific finite difference in time is written as[36]:

$$f_i(\mathbf{x}+c_i\Delta t, t+\Delta t) - f_i(\mathbf{x},t) = \Omega(\mathbf{x},t) \tag{1}$$

Here, the left-hand side of $f_i(\mathbf{x}, t)$ is the particle distribution function in direction i at position $\mathbf{x}$, and $\mathbf{c}_i$ is the discretized velocity vector of the particle moving in direction i. The collision term on the right side $\Omega(\mathbf{x}, t)$ is defined by the Bhatnagar–Gross–Krook (BGK) model, which is a simple linearized collision term[37]:

$$\Omega(\mathbf{x},t) = -\frac{1}{\tau}[f_i(\mathbf{x},t) - f_i^{eq}(\mathbf{x},t)] \tag{2}$$

where τ is the relaxation time toward equilibrium. It is determined by the viscosity of the fluid and discretized spatial and temporal intervals as follows:

$$\nu = \frac{2\tau - 1}{6}\frac{(\Delta x)^2}{\Delta t} \tag{3}$$

$f_i^{eq}(\mathbf{x},t)$ is the local equilibrium distribution function. For low-Mach number flows, the Maxwell-Boltzmann equilibrium distribution is conventionally used[38]. This is approximated using a second-order expansion as follows:

$$f_i^{eq}(\mathbf{x},t) = \omega_i \rho \left[1 + \frac{3\mathbf{c}_i \cdot \mathbf{u}}{c^2} + \frac{9(\mathbf{c}_i \cdot \mathbf{u})^2}{2c^4} - \frac{3|\mathbf{u}|^2}{2c^2} \right] \tag{4}$$

where ρ is the fluid density, $\mathbf{u}$ is the velocity, ω_i is the weight factor in the i direction.

$$\omega_i = \begin{bmatrix} \frac{2}{36} & (i = 1,...,6) \\ \frac{1}{36} & (i = 7,...,18) \\ \frac{12}{36} & (i = 19) \end{bmatrix} \tag{5}$$

From the distribution function, it is straightforward to obtain macroscopic variables such as fluid density ρ and velocity $\mathbf{u}$ through the following equations.

$$\rho(\mathbf{x},t) = \sum_i f_i(\mathbf{x},t) \tag{6}$$

$$\rho\mathbf{u}(\mathbf{x},t) = \sum_i \mathbf{c}_i f_i(\mathbf{x},t) \tag{7}$$

PowerFLOW, utilizing the unsteady LBM approach, employs VLES. LBM-VLES serves as a tool for the prediction of both the aerodynamic forces and aeroacoustic noise generated by aircraft. VLES, in this context, stands as a turbulence modeling method specially crafted for the analysis of large-scale unsteady flow fields[36]. It is a hybrid approach of RANS/LES and Detached Eddy Simulation, which was developed to overcome the limitation that RANS is incapable of capturing turbulent instability effects, and LES can be too computationally expensive when the resolution of only the relatively larger scale is required[39]. In the LBM analysis for turbulence modeling, it is necessary to calculate the relaxation time to consider the turbulence effects in addition to the viscosity relaxation time of the BGK model. The turbulence relaxation time is a function of the turbulent kinetic energy (k) and turbulent dissipation rate (ε). These are obtained by the solution of a variant of the Renormalization group (RNG) $k-\varepsilon$[36], referred to as LBM-VLES. The turbulent kinetic energy (k) and turbulent dissipation (ε) are applied to locally adjust the turbulent viscosity relaxation time:

$$\tau_{eff} = \tau + \tau_{eddy} = \tau + C_\mu \frac{k^2/\varepsilon}{T\sqrt{1+\tilde{\eta}^2}} \tag{8}$$

where $C_\mu = 0.09$, η is based on a local strain parameter, a local vorticity parameter, and local helicity parameters[40].

B. LBM simulation setup

More complex interactions are present in full realistic aircraft. As a result of the literature[20,41,42], it was observed that the mutual interactions between additional components (e.g., rotor, fuselage, hub, mast, canard, landing gear) affected the aerodynamic and acoustic characteristics of the vehicle. However, in this study, the computational analysis of a simplified rotor-airframe configuration was conducted to investigate the rotor-airframe interaction in detail, and validation work was performed against available measurements. This study used a two-bladed DJI 9443 rotor with a diameter of 0.24 m (9.45 in.) to validate the aerodynamic and aeroacoustic simulation data[43]. The planform geometry, chord, and twist angle distributions as functions of the radial position are shown in Figs. 2 and 3, respectively. A cylindrical airframe maintains a consistent cross-section in the longitudinal direction, while a conical airframe features an expanding cross-section starting from the rotor hub to the tip. The airframe components were vertically positioned at distances of 0.1, 0.3, and 0.5R vertically below the 1/4-chord location of the rotor tip, as shown in Fig. 4. Here, *R* represents the radius of the rotor blade.

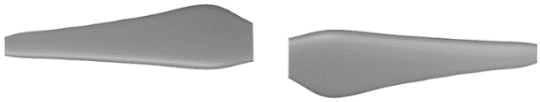

FIG. 2. Planform geometry of DJI 9443 propeller

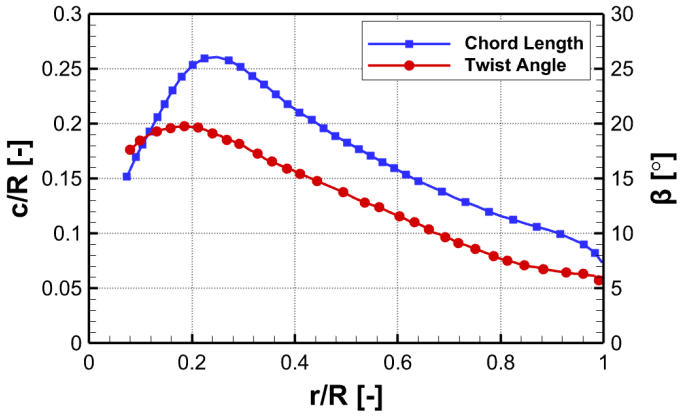

FIG. 3. Chord and twist angle distributions of DJI 9443 propeller

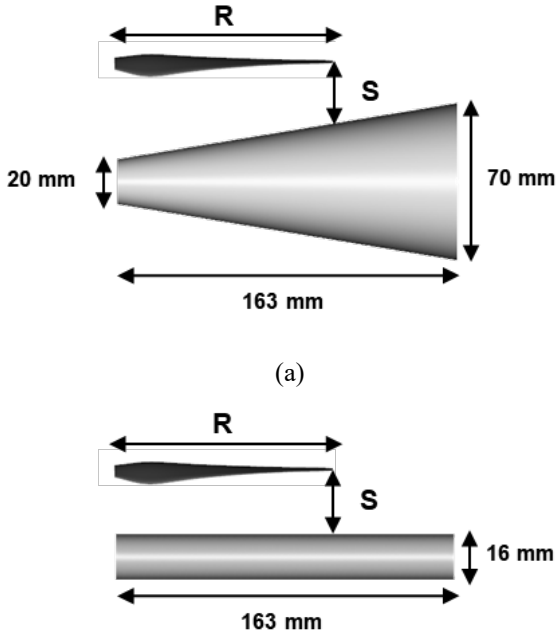

FIG. 4. Geometry of airframe: (a) conical airframe, (b) cylindrical airframe

Figures 5 and 6 illustrate the computational domain for the interaction between the rotor and airframe, as well as the grid system in close proximity to the rotor blades. The computational domain is composed of hexahedral cells or voxels that fully encompass both the rotor blade and the airframe. The domain size was 35 times the rotor diameter (D) for both the isolated rotor and rotor-airframe cases. In this study, the FW-H acoustic analogy method, incorporating a permeable surface, was employed to calculate the noise levels radiated from the rotor-airframe configuration. The permeable FW-H method can consider thickness noise, load noise, and flow-induced noise, facilitating efficient calculations by substituting the volume integration required for evaluating flow-induced noise with surface integrals over permeable surfaces. A virtual permeable surface has been applied to encompass both the surface noise sources (the rotor blades and airframe) and the volume noise source (the flow field). The size and position of the permeable surface are illustrated in Fig. 6. Arbitrary boundary surfaces in the form of cubes were constructed within the domain, and the grid resolution was managed using a specific set of variable resolution (VR) values. A voxel in a given resolution region was updated twice as often as a voxel in a nearby region with lower resolution. In this study, the VR regions for the isolated rotor and rotor-airframe were divided into 16 and 15 regions, respectively, and the VR configuration and level were designed differently to consider computational cost. The height of the first-layer cell is 0.2 mm, corresponding to 1.4% of the chord length at a 75% tip radius. The finest grid region in the proximity of the rotor blade and airframe is composed of 15 layers with the height of

the first-layer cell. The stationary airframe and the rotating rotor blades are separated using the sliding mesh method, enabling the moving mesh to shear and slide relative to the stationary mesh along the interface. A viscous adiabatic wall boundary condition was applied to the surfaces of the rotor blade and airframe, while the far-field boundary condition was imposed on the surfaces of the computational domain. Because this is a hovering condition, the free-stream velocities in the x-, y-, and z-directions were set to zero. Standard ambient temperature and pressure conditions were utilized, and no-slip boundary conditions were enforced on both the rotor and airframe surfaces to account for the effects of viscosity.

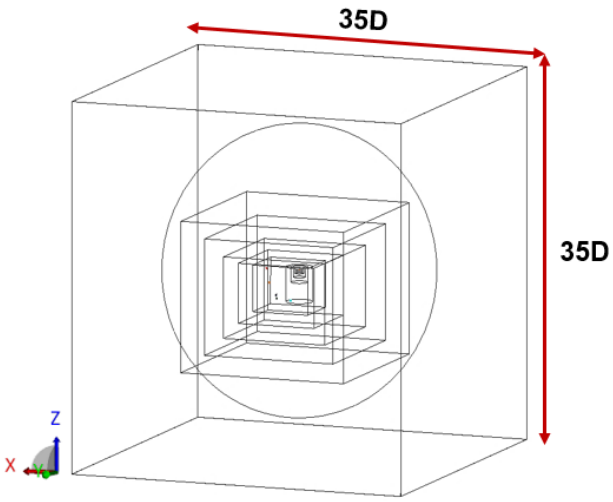

FIG. 5. Computational domain for LBM simulations

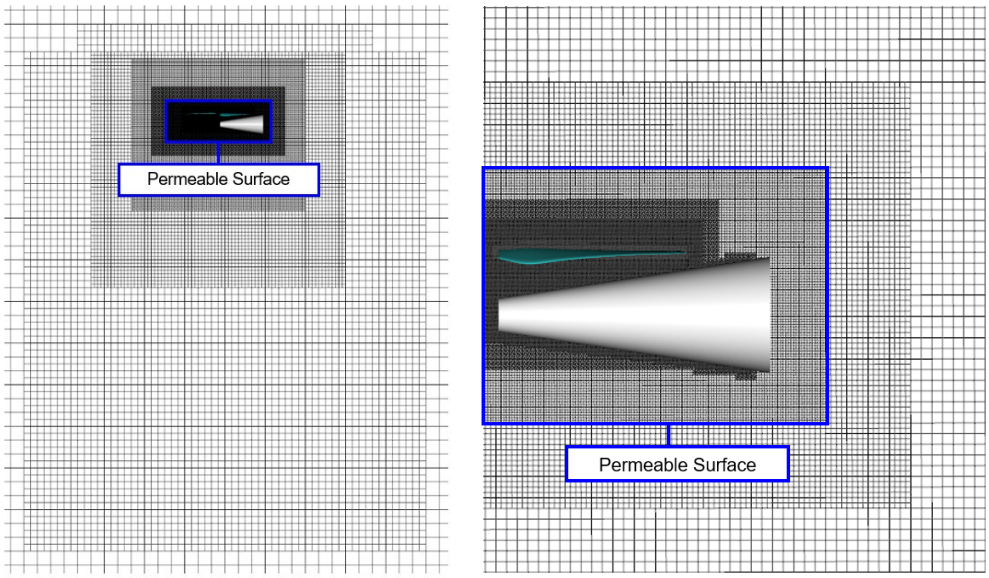

FIG. 6. Computational grid system for rotor-conical airframe configuration (left) and grid resolution around the rotor blade and airframe (right)

The computational test conditions are presented in Table 1. The simulation was carried out at various rotor speeds: 4800, 5400, and 6000 RPM for the isolated rotor, for which experimental data exist, to validate the accuracy of the numerical method used in this study. LBM simulations were performed at a rotor speed of 5400 RPM for the conical airframe, chosen as the reference airframe, to investigate the variations in aerodynamic and noise characteristics depending on the separation distance between the rotor blade and airframe. Furthermore, the flow field and noise characteristics of the cylindrical airframe were compared to those of the conical airframe through simulations conducted at 5400 RPM and $S/R = -0.1$, where the negative tip clearance means that the airframe is below the rotor. The chosen tip clearances for this study were selected because they closely resemble the typical rotor-airframe spacing found in common multicopter vehicles[15].

TABLE 1. Computational testing conditions

Case	Ω (RPM)	S/R
Isolated rotor	4800, 5400, 6000	N/A
Rotor-conical airframe	5400	−0.1, −0.3, −0.5
Rotor-cylinder airframe	5400	−0.1,

The flow conditions for the computational simulations are listed in Table 2. The Reynolds number, referred to as Re_c (0.75R), was calculated based on the chord at a 75% tip radius. The simulation was conducted over 25 rotor revolutions to ensure the same frequency resolution (Δf) of noise data as the measurements[43]. It was computed at every 0.01° azimuth angle, and the computational domain was internally determined by PowerFLOW, utilizing a Courant-Friedrichs-Lewy (CFL) number of 1, which is based on the finest voxel size[25]. Convergence of the isolated rotor thrust level was established to happen by the 7th revolution, and similar amplitude variations in thrust were periodically observed in the rotor-airframe cases. Therefore, the data after the 7th rotation were used for the analysis.

TABLE 2. Flow conditions

Properties	Values
Flight condition	Hover
Rotating speed, Ω	4800 RPM ~ 6000 RPM
Reynolds number, Re_c (0.75R)	$4.5 \times 10^4 \sim 5.7 \times 10^4$
Tip Mach number, M_{tip}	0.177 ~ 0.221

C. Acoustic simulation setup

The LBM is inherently compressible and provides a solution to unsteady flow, allowing for the direct computation of noise generated by unsteady flow around a rotating body[44]. Nevertheless, when the observer is positioned at a considerable distance from the source region, creating a fine grid at the observer's location becomes necessary for accurate noise prediction. However, this proves to be impractical due to the exceptionally high computational cost[45]. Furthermore, the turbulence term, represented as a quadruple source, involves volume integration. To consider this, it is necessary to perform volume integration across the noise sources in the region that includes the rotor-airframe configuration. Nonetheless, when compared to surface integration, the computational efficiency of volume integration for acoustic pressure data within a flow field is lower. Hence, a hybrid approach must be used to predict the far-field noise radiation. In this approach, the computational domain is split into different regions such that the acoustic field or flow field can be solved using different equations and numerical techniques. In this study, the Ffowcs Williams-Hawkings (FW-H) acoustic analogy method, which is a hybrid method, is employed for far-field noise prediction. Furthermore, the FW-H acoustic analogy method, incorporating a permeable surface, was employed to account for the effects of surface noise sources (thickness noise and loading noise) and volume noise sources (flow-induced noise). The volume integration used to assess flow-induced noise can be replaced with surface integration over permeable surfaces, enhancing computational efficiency. Farassat formulation 1A using the virtual permeable surface, which is a solution for an arbitrary moving surface of the FW-H equation, can be represented as follows:

$$p'_T(\mathbf{x},t) = \frac{1}{4\pi}\int_{f=0}\left[\frac{\rho_0(\dot{v}_n + v_n)}{r\left|1-M_r\right|^2}\right]_{ret} dS + \frac{1}{4\pi}\int_{f=0}\left[\frac{\rho_0 v_n (r\dot{M}_r + a_0 M_r - a_0 M^2)}{r^2\left|1-M_r\right|^3}\right]_{ret} dS \tag{9}$$

$$p'_L(\mathbf{x},t) = \frac{1}{4\pi a_0}\int_{f=0}\left[\frac{\dot{l}_r}{r\left|1-M_r\right|^2}\right]_{ret} dS + \frac{1}{4\pi}\int_{f=0}\left[\frac{l_r - l_M}{r^2\left|1-M_r\right|^2}\right]_{ret} dS + \frac{1}{4\pi a_0}\int_{f=0}\left[\frac{l_r (r\dot{M}_r + a_0 M_r - a_0 M^2)}{r^2\left|1-M_r\right|^3}\right]_{ret} dS \tag{10}$$

where a_0 is the speed of sound, ρ_0 is the density of air, and M_r is the velocity component in the radiation direction normalized by the speed of sound. The term which has the subscript (i.e., $\dot{v}_n$ and $\dot{l}_r$) indicates the source time (τ) derivative. This method enables the prediction of all noise sources, including monopole, dipole, and quadrupole sources[4]. The terms enclosed in [] were evaluated at a retarded time[46]. Because the wave equation is defined with respect to the source time, the acoustic pressure at the observer's position ($\mathbf{y}$) requires a physical

distance between the noise source ($\mathbf{x}$) and the observer. The relationship between the source time and observer time (t) is defined by the following relationship:

$$\tau = t - \frac{r}{a_0} = t - \frac{|\mathbf{x} - \mathbf{y}|}{a_0} \tag{11}$$

In this study, five microphones were placed at a radial distance of 1.905 m from the rotor axis[15,43], as shown in Fig. 7. To analyze the influence of the rotor-airframe interaction, the microphone array was divided into elevation and azimuthal sub-arrays, the angular locations of which are defined in Table 3. Microphones M1, M2, and M3 were located at elevation angle intervals of 22.5° from the plane of the rotor, and M4 and M5 were set at azimuth angle increments of 45° counterclockwise from M3.

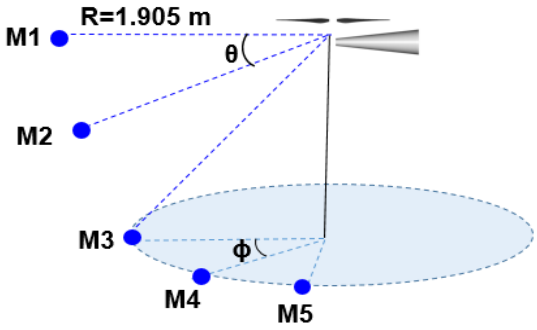

FIG. 7. Definition of microphone positions, azimuth (ϕ) and elevation (θ) angles

TABLE 3. Locations of microphone

Mic.	(θ, ϕ)
M1	(0.0°, 0.0°)
M2	(−22.5°, 0.0°)
M3	(−45.0°, 0.0°)
M4	(−45.0°, 45.0°)
M5	(−45.0°, 90.0°)

3. RESULTS AND DISCUSSION

A. Validation

Before delving into the investigation of the interaction between the rotor and airframe and their impact on rotor aerodynamics and noise, validation studies were conducted for both the isolated rotor and rotor-airframe

configurations. In the case of an isolated rotor under hovering flight conditions, one of the primary sources of rotor noise is the loading noise generated by the aerodynamic forces acting on the surfaces of the rotating blades. As a result, the integrated thrust forces of the isolated rotor were predicted and compared with experimental data obtained from the NASA Langley Research Center[43] prior to conducting noise validation. The LBM simulations were executed at rotor speeds of 4800, 5400, and 6000 rpm, and corresponding experimental results were gathered. The validation results reveal that the predictions for the thrust force of the isolated rotor are underestimated, by approximately 3%–9%, for all rotor speeds, as indicated in Fig. 8. The rotor blades used in this study are designed for small-scale UAVs, resulting in a small size and a low Reynolds number. Therefore, it was difficult to accurately predict the thrust performance of the rotor blade through computational analysis. Although the difference of 3%–9% could be large, compared to high-fidelity CFD prediction within a margin of 3%, the error was smaller compared to results from other previous studies conducted by Thurman *et al*.[25]

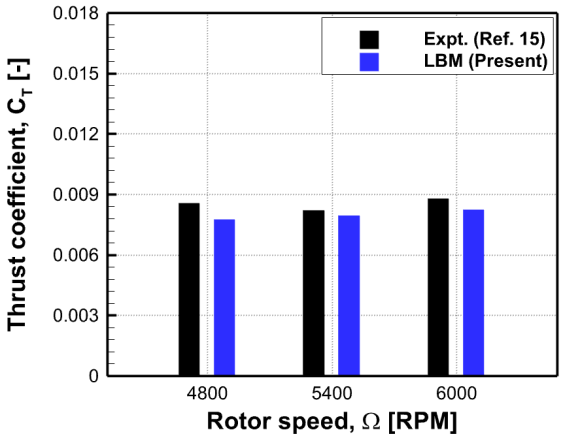

FIG. 8. Comparison of thrust coefficient between LBM simulations and measurements

Loading noise and thickness noise, being deterministic elements of rotor aerodynamic noise, generate significant acoustic amplitudes at the blade passage frequency (BPF) and its related harmonics. Consequently, the tonal noise components at the primary rotor-related frequencies play a pivotal role in determining the overall noise levels of the isolated rotor. The amplitude of tonal noise associated with BPF and its harmonics with CFD predictions provided by the work of Zawodny and Boyd[15] was compared to verify the predictive capability of LBM simulations as shown in Figures 9, 10, and 11. For the 1st BPF directivity in Fig. 9, all predicted noise levels were within a difference error relative to the experimental data of 2.6 dB. Although the increase in noise intensity with RPM and the noise directivity with respect to angles exhibit excellent agreement, a difference error relative

to the experimental data is 2.6 dB. However, it shows better results than the PAS prediction, which has a maximum error of 3.1 dB. Furthermore, LBM has a disparity with measurements within 2 dB at all microphone positions. It indicates that the present method has the capability of accurately predicting the aerodynamic noise. Even if quite substantial disparity between the numerical prediction and the measured data for the 2nd directivity was also observed in Fig. 10, these numerical errors have been reported in previous studies[6,25,43]. Owing to the phase cancellation effect between the thickness and loading noise, a trough was observed at approximately 22.5° at rotating speeds of 4800 rpm and 5400 rpm, and LBM simulation shows a better result than the CFD prediction given in the work of Zawodny and Boyd[15]. Notably, the amplitudes of the BPF harmonics in Fig. 11 aligned closely with the measurements for all the microphone locations as defined in Fig. 7. Especially, the difference of tonal noise levels at the 1st–5th BPF harmonics is within 1 dB at M1 position. Furthermore, even though predicting the noise at higher BPF harmonics with a numerical simulation is a challenging problem in general, the noise levels at all microphone locations were similar to the experimental data even at higher harmonics compared to the CFD prediction. The validation works for both the isolated and rotor-airframe configurations show that the numerical results obtained from LBM simulations with permeable FW-H acoustic analogy are validated against available measurements and CFD predictions.

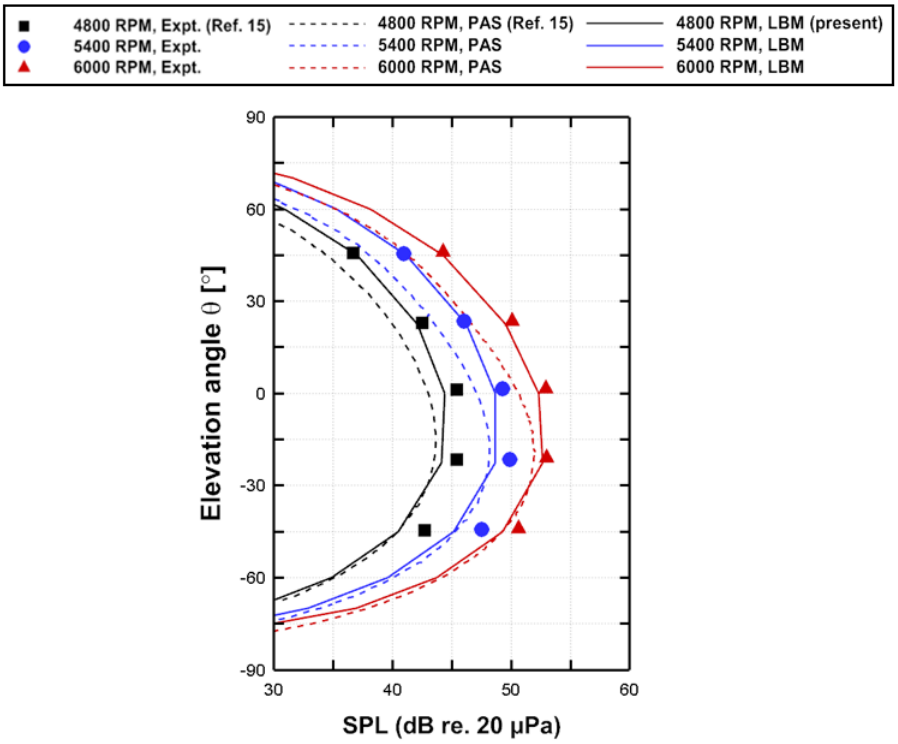

FIG. 9. Comparison of 1st BPF directivity between LBM simulations and measurements

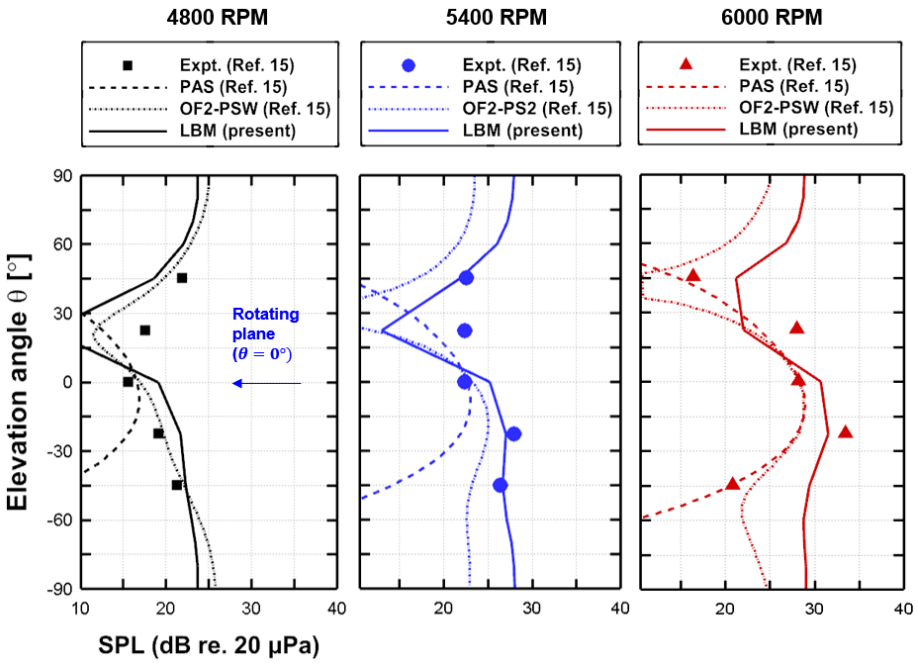

FIG. 10. Comparison of 2nd BPF directivity between LBM simulations and measurements

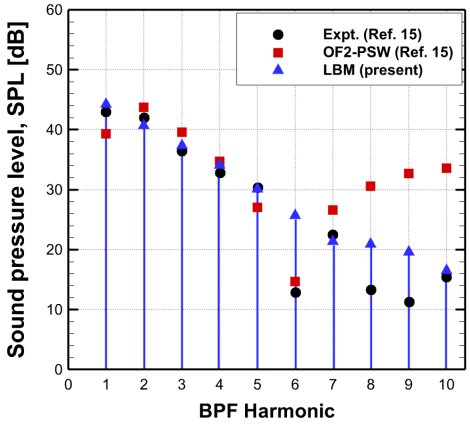

(a)

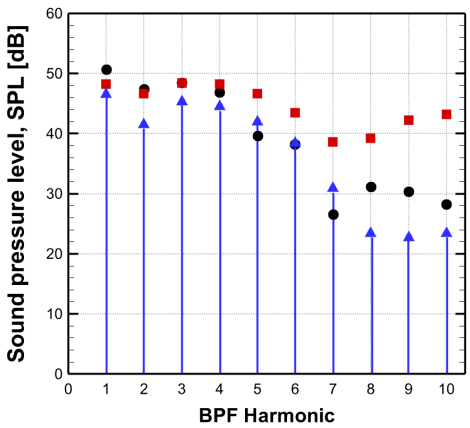

(b)

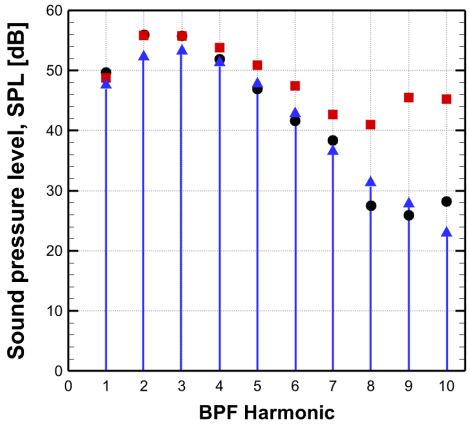

(c)

FIG. 11. Comparison of the amplitude of BPF harmonics between LBM simulations and measurements for conical airframe case: (a) M1, (b) M3, and (c) M5 locations

B. Effects of the airframe shape on aerodynamics and acoustics

This section presents the effects of airframe shape on the flow and acoustic fields. Figs. 12(a) and 12(b) show the mean thrust data for the last five revolutions and one revolution, respectively. They represent little thrust fluctuation for an isolated rotor. However, in the presence of the airframe, distinct thrust fluctuations of 2/rev are observed during the specific phase ($\psi = 1440°, 1620°, 1800°$) when the blade passes directly over the airframe. Additionally, there is a slight rise in the rotor thrust levels due to the partial ground effect[15]. The average thrust level increased by 2.15% for the conical airframe case compared to the cylindrical airframe case. This is likely because a conical airframe, with its larger volume and surface area, has a greater influence on the flow in the direction of the wake convection.

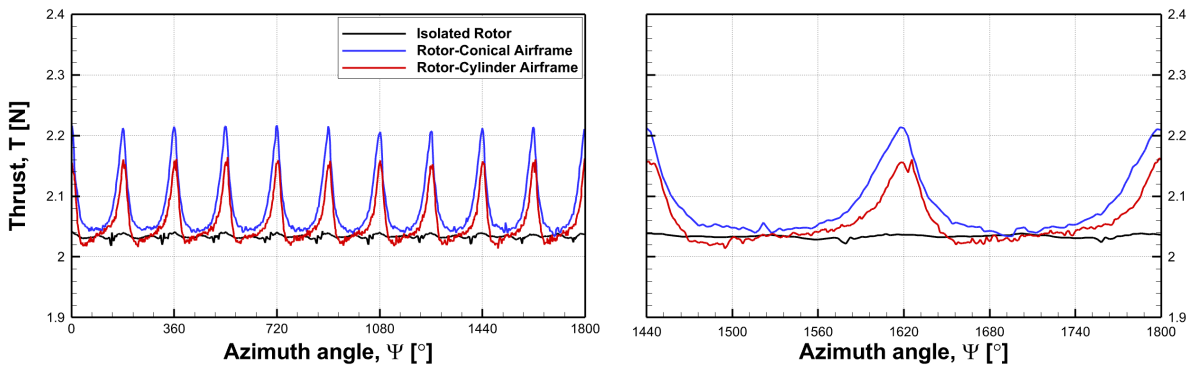

(a) (b)

FIG. 12. Comparison of time-history of thrust forces between rotor-airframe and isolated rotor configurations: (a) 5 rev. and (b) 1 rev.

In Figure 13, the thrust levels across the three cases were examined based on the results of the rotor surface pressure distribution. The impact of the rotor-airframe interaction on the pressure distribution along the rotor blade surface was analyzed at the instantaneous phase when the rotor blade passes over the airframe. As depicted in Fig. 11, the airframe is positioned below the rotor blade, resulting in a significant influence of the rotor-airframe interaction effects on the lower blade surface rather than on the upper surface. Moreover, the conical airframe resulted in a greater pressure difference between the upper and lower surfaces of the rotor blades than that of the cylindrical airframe. This finding is consistent with a prior observation of higher thrust levels in a conical airframe.

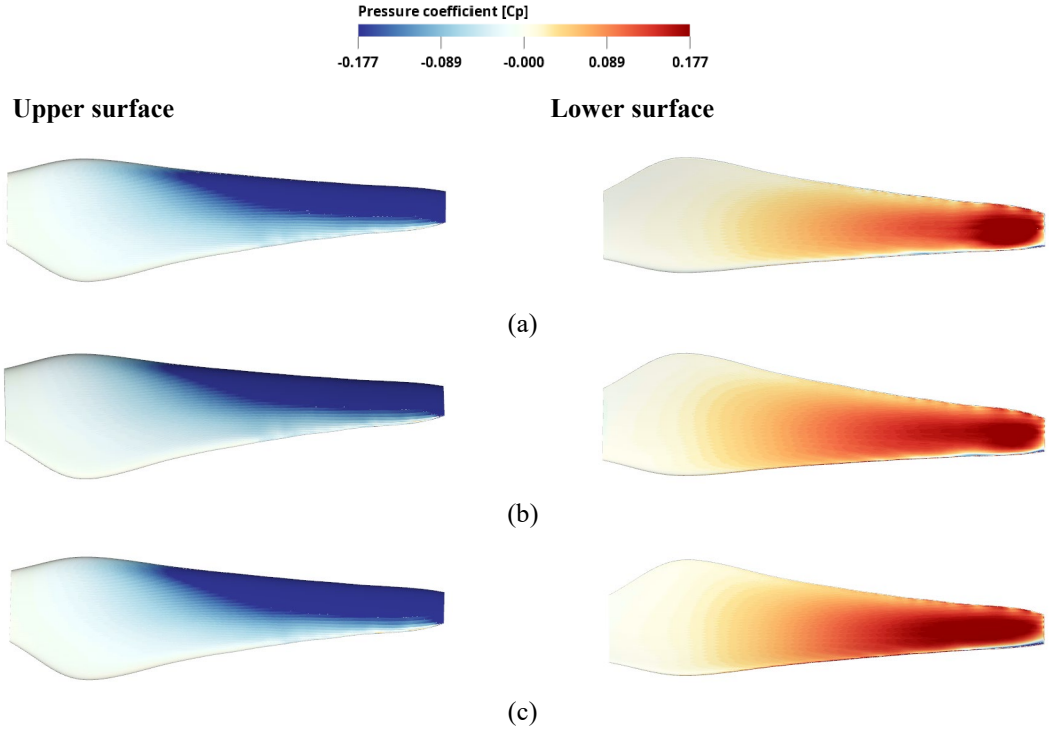

FIG. 13. Comparison of instantaneous pressure coefficient contours on the upper surface (left) and lower surface (right) : (a) isolated rotor, (b) rotor-cylinder airframe, (c) rotor-conical airframe

In Figure 14 (left), the noise spectra for the different airframe cases under hovering conditions are presented. This illustrates that substantial noise with high amplitude is generated at both the BPF and its harmonics, indicating that the BPF is the dominant frequency component contributing to the rotor noise. Fig. 14 (right) shows a more detailed analysis of the BPF and harmonic amplitude. Microphone M1 is located in the rotor in-plane area, where thickness noise predominantly contributes, and the highest harmonic amplitude was observed in the conical

airframe case, except for the 1st BPF. Even if the thickness remains constant, the in-plane force component acting on the airframe was more pronounced in the conical airframe than in the cylindrical airframe due to the strong wake interaction in the edgewise direction. It can be explained that a conical shape has the potential to increase in-plane noise, even though the thickness remains constant. This trend was observed at the M3 and M5 microphones up to the 5th BPF. It can be explained by the highest thrust level in the conical airframe case, which led to a high sound pressure level associated with the low-frequency loading noise. After the 5th BPF, it is observed that the cylindrical airframe case results in a higher harmonic amplitude, believed to be related to the noise generated primarily due to the blade wake-airframe interaction, particularly across the frequency range of 1 kHz $< f <$ 2 kHz. The primary frequency range of the blade wake-airframe interaction noise is 1 kHz $< f <$ 2 kHz (larger than 5th BPF), and wake structure plays a crucial role in determining its magnitude. It can be seen that a cylindrical airframe has substantially less dissipation in the wake structure compared to a conical airframe, resulting in higher sound pressure after the 5th harmonic (The rotor-airframe interactional effects on the evolution of wake structure will be discussed in Fig. 16).

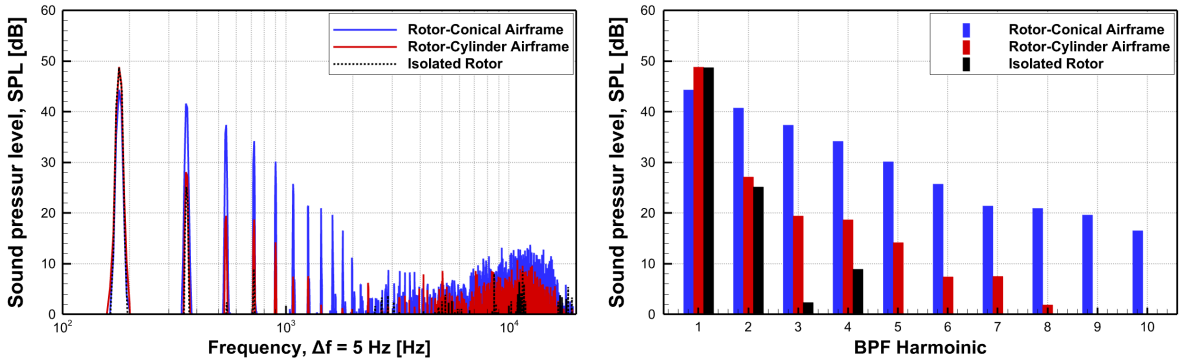

(a)

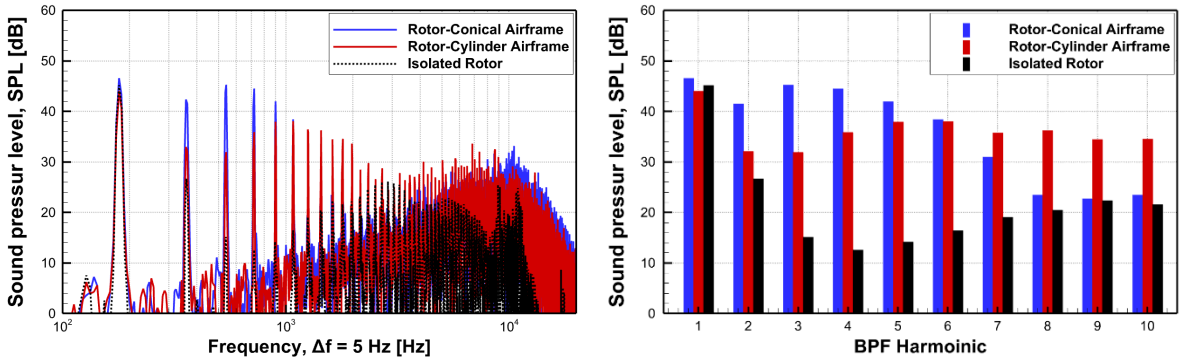

(b)

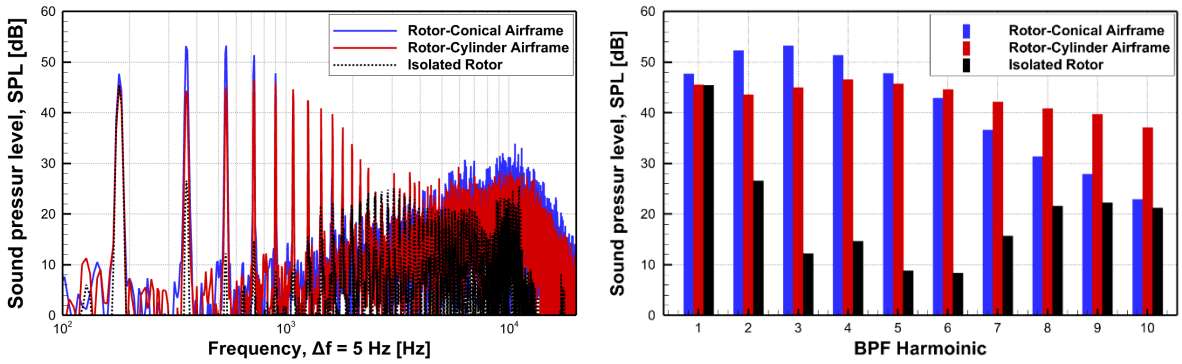

(c)

FIG. 14. Acoustic narrowband spectra (left) and BPF harmonics (right) comparisons between rotor-airframe and isolated rotor configurations: (a) M1, (b) M3, and (c) M5 locations

In Figure 15, the surface dB map illustrates the dominant surface locations of the noise at the phase when the blade passes over the airframe. To create the surface dB map, surface decibels are calculated through post-processing techniques based on the results of the LBM analysis. This method allows us to identify the dominant noise radiation locations and amplitudes on the surfaces of the rotor blade and airframe at specific frequency bands by calculating the power spectrum pressure using the flow variables computed on the surfaces. We used data with surface variable information of the rotor blade and airframe, with a frequency resolution of 5 Hz. In the case of rotor noise, tonal noise was more dominant than broadband noise; thus, a frequency range that included the first two BPF was chosen. For an isolated rotor case, the 1st BPF was predicted to generate an SPL approximately 10 dB greater than the 2nd BPF at a 20%–40% span. However, when the airframe was present, it was observed that the noise radiated from the rotor and airframe was higher at the 1st BPF. Specifically, the acoustic amplitude of the conical airframe was significantly higher owing to the larger area of the airframe surface. Furthermore, within the frequency range, including the 1st BPF, the acoustic amplitudes of the rotor with a conical airframe were notably greater than those of the rotor with a cylindrical airframe along the blade leading edge. Finally, through analysis of the surface dB map, it can be assumed that the noise radiating from the airframe is influenced by the wake interacting with the airframe rather than by the tip vortex.

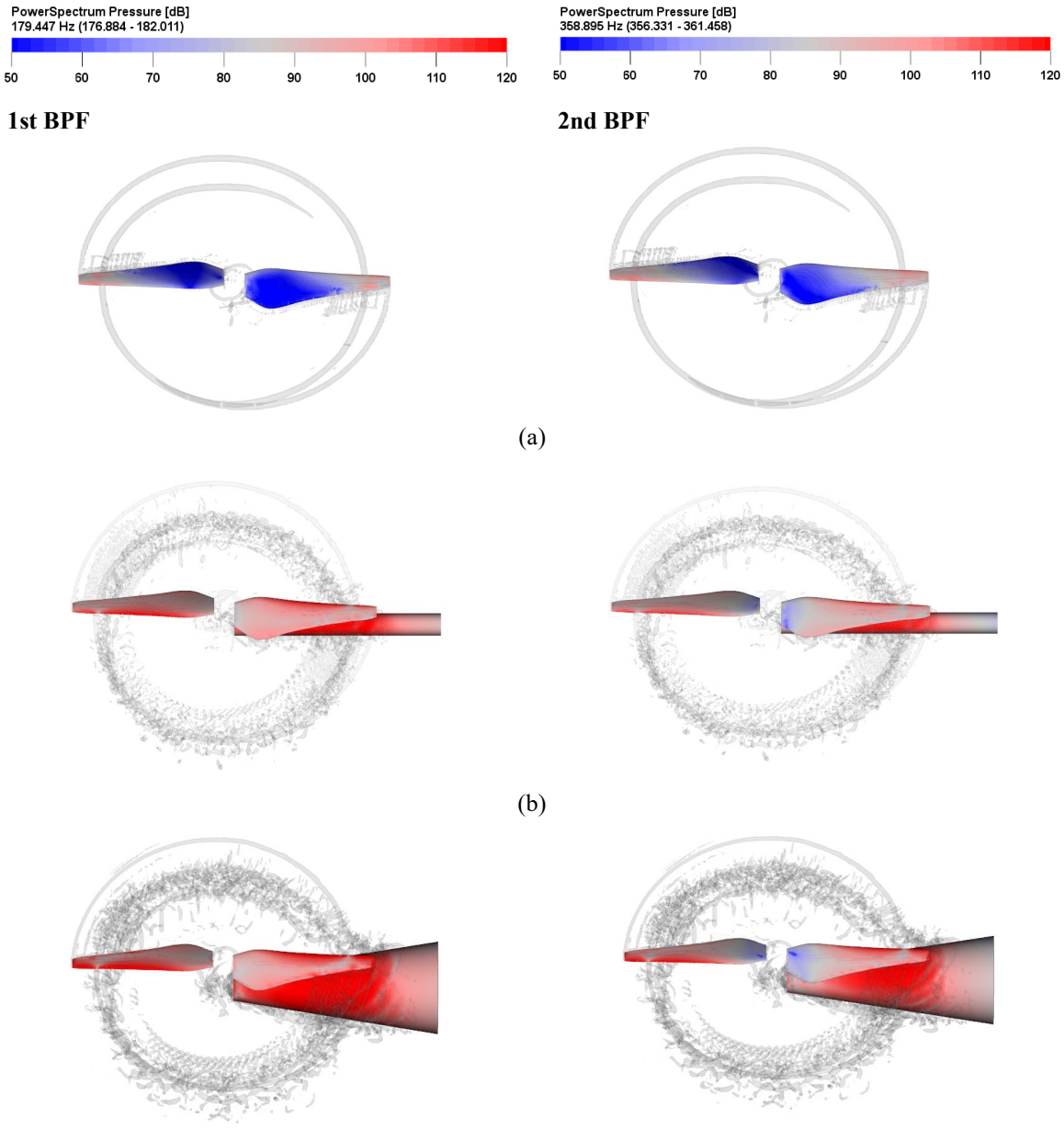

FIG. 15. Comparison of dB surface map at 1st BPF (left) and 2nd BPF (right): (a) isolated rotor, (b) rotor-cylinder airframe, (c) rotor-conical airframe

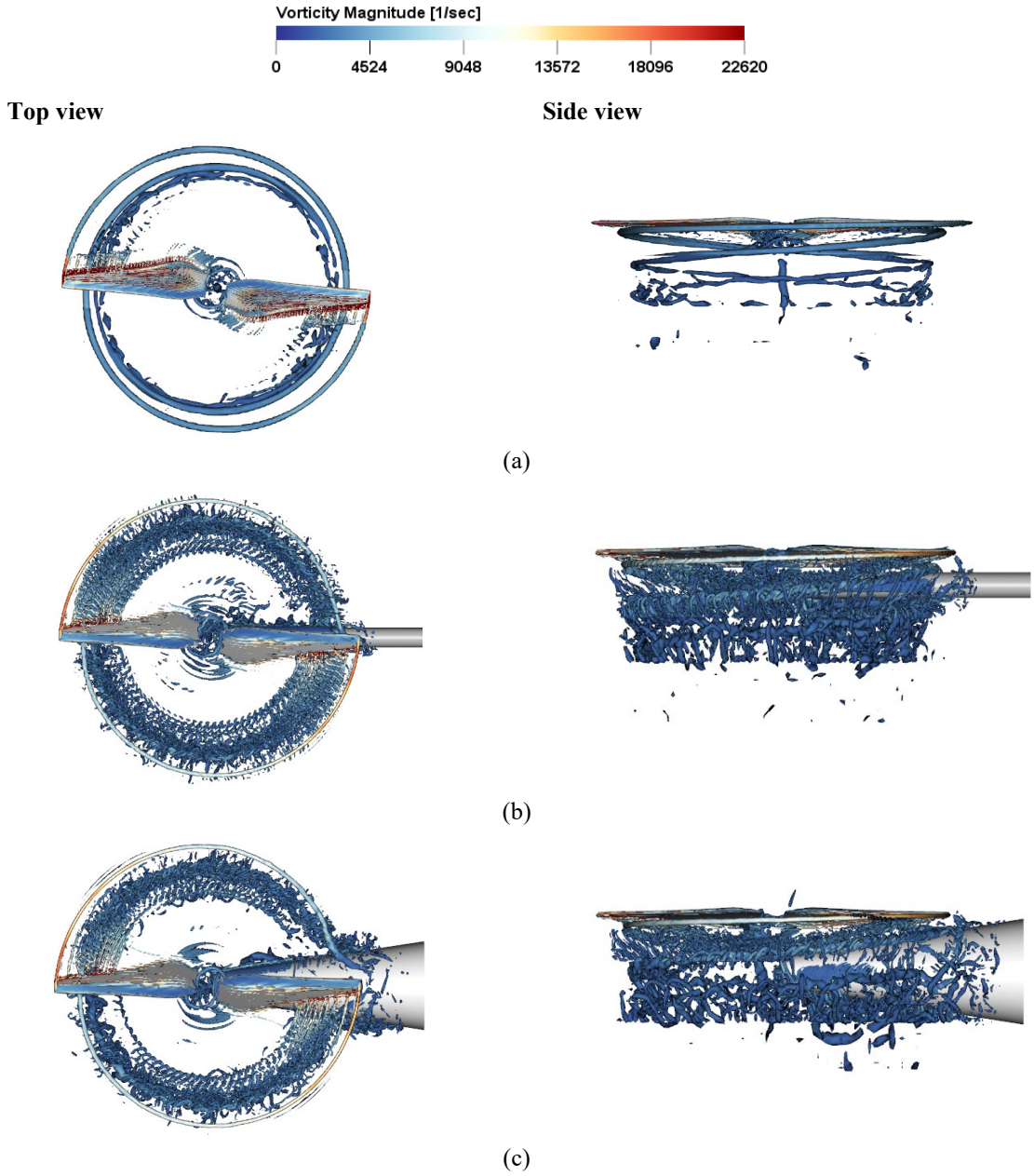

FIG. 16. Comparison of rotor wake visualized by iso-surfaces of the Lambda-2 criterion: (a) isolated rotor, (b) rotor-cylinder airframe, (c) rotor-conical airframe

Figure 16 shows the prediction of wake structure based on the effects of the airframe and its shape. The wake structures are presented separately in both top and side views. In the case of an isolated rotor in hovering, a distinct helical wake structure forms and develops downward. Because no component influenced wake development, a symmetrical structure was formed. However, regardless of the airframe configuration, an asymmetrical wake structure develops when the airframe exists due to the rotor-airframe interaction. In addition, the tip vortex breakdown phenomenon, in which the helical structure decays, occurs in the early stages, resulting in the

generation of a turbulent wake. When a conical airframe is present, the dissipation of the wake structure after the wake collides with the airframe occurs more rapidly than when a cylindrical airframe is present.

C. Effects of the separation distance on aerodynamics and acoustics

In this section, we explored the impact of rotor-airframe interaction on the flow field and noise at different rotor tip clearances. Fig. 17 shows the effects of rotor-airframe interaction on rotor thrust in hover. In the case of the smallest rotor tip clearance, $S/R = -0.1$, significant thrust force fluctuation is observed due to the rotor-airframe interaction influence. However, thrust amplitudes decrease substantially as the distance increases. Finally, in the case of $S/R = -0.5$, a similar trend to that of an isolated rotor is observed. Furthermore, in the case of $S/R = -0.1$, the thrust value is maximum when the rotor blade passes over the airframe (ψ = 1440°, 1620°, 1800°); however, as the distance between the airframe and rotor tip increases, the impact of the airframe on the thrust value shows a notable reduction. Fig. 18 presents the wake structure prediction results for various rotor tip clearances. A strong tip vortex generated from the blade tip develops in a helical structure and propagates axially downstream in the isolated rotor case. However, in the airframe case, the interaction between the rotor blades and the airframe influences the development of the wake structure. In the case of $S/R = -0.1$, the tip vortex collides with the airframe before it is fully developed. Especially for $S/R = -0.3$ and -0.5, it was observed that the rotor wake does not exhibit distinct structures and disperses along the airframe surface. Some wakes collide with each other, giving rise to a turbulent wake that ascends, forming a fountain flow. In Fig. 17(b), as the rotor blades directly pass over the airframe, unlike the case of $S/R = -0.1$, there is a tendency for the thrust to slightly decrease, and an increase for the case of $S/R = -0.3$ and -0.5, which is believed to be the resultant effect of the fountain flow. Additionally, with increasing rotor tip clearance, the instability and unsteadiness of the root wake structure are weakened.

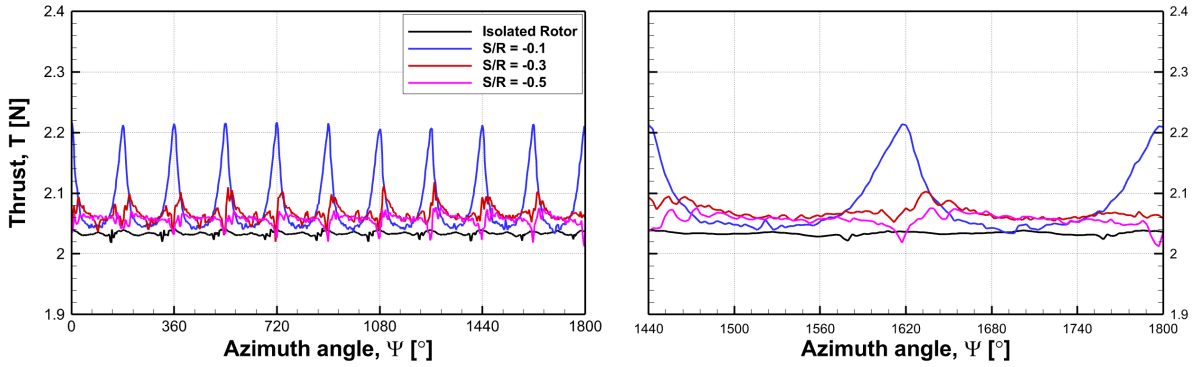

(a) (b)

FIG. 17. Comparison of time-history of thrust forces between isolated rotor and rotor-conical airframe configurations with different separation distances: (a) 5 rev., (b) 1 rev.

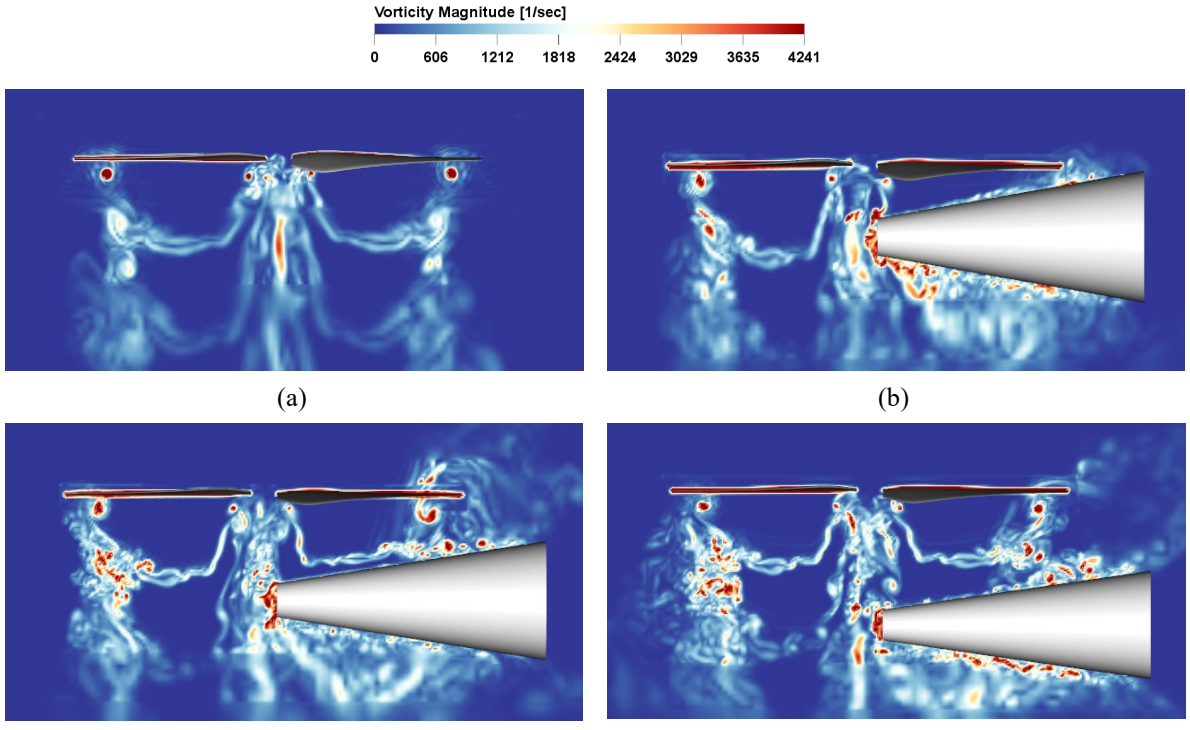

(a) (b)

(c) (d)

FIG. 18. Comparison of vorticity magnitude contours between isolated rotor and rotor-conical airframe configurations with different separation distances: (a) isolated rotor, (b) *S/R* = −0.1R, (c) *S/R* = −0.3, (d) *S/R* = −0.5

Figure 19 shows the SPL graphs for microphones M1, M3, and M5 at different rotor tip clearances. For M1 and M3, comparable noise levels were observed regardless of the airframe presence and rotor-airframe separation distance at the 1st BPF. Even though thickness noise directivity is dominant for the M1 position and steady loading noise directivity is dominant for M3, this outcome is most probably attributed to the fact that the average thrust

experiences only a minor decrease as the gap between the rotor and the airframe widens. Furthermore, after the 2nd BPF, the sound pressure level decreased with increasing distance between the airframe and rotor tip, regardless of the microphone location. Because the directivity of the loading noise is more prominent at M3 in comparison to M1, the graph shows an increased sound pressure level, and the largest tonal amplitude is observed at M5, which is perpendicular to the center plane of the airframe.

Next, for the comprehensive noise comparison based on the rotor tip clearance, Fig. 20 provides a comparison of overall sound pressure level (OASPL) concerning the elevation and azimuth angles; the azimuth angle here is −45° elevation angle location. There is a maximum noise level increase of 12 dB at $S/R = -0.1$ compared to the isolated rotor, and it is comparable to the noise levels at $S/R = -0.3$. Furthermore, in comparison to the noise level of the blade in-plane area, it increased by more than 10 dB at the elevation angle, where the unsteady loading noise and turbulent noise effects increased. For $S/R = -0.1$, there was an azimuthal variation in the noise level around 4 dB, while for $S/R = -0.3$ and $S/R = -0.5$, it was within approximately 1 dB.

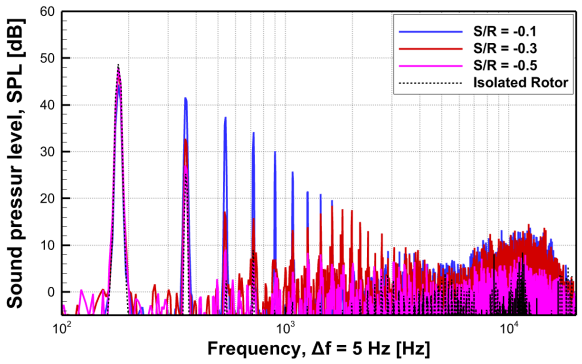

(a)

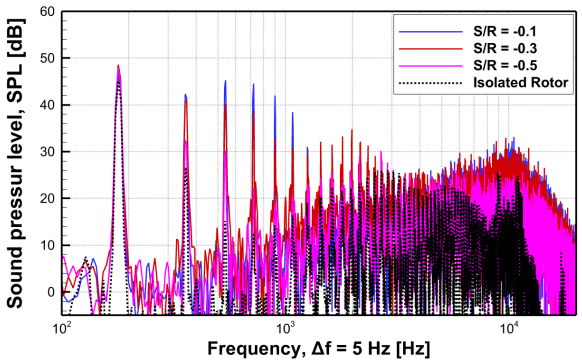

(b)

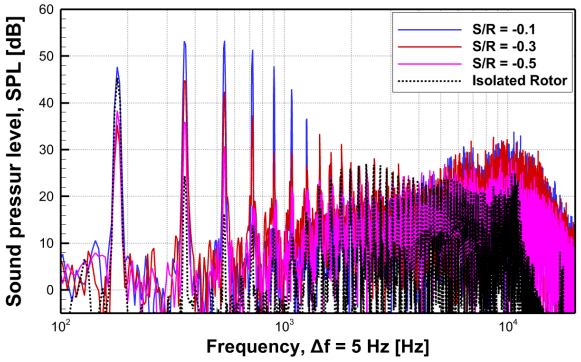

(c)

FIG. 19. Comparison of acoustic narrowband spectra between isolated rotor and rotor-conical airframe configurations with different separation distances: (a) M1, (b) M3, and (c) M5 locations

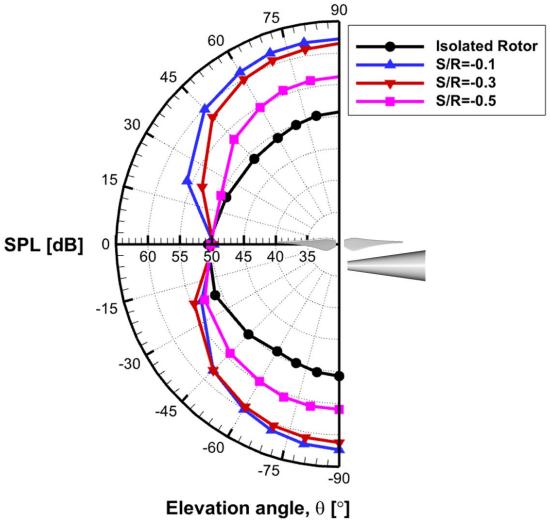

(a)

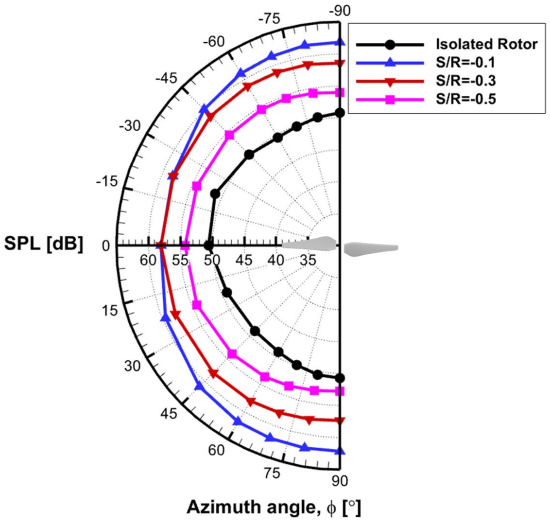

(b)

FIG. 20. Comparison of overall sound pressure level (OASPL) directivity between the isolated rotor and rotor-conical airframe with different separation distances: (a) elevation angle, (b) azimuth angle

In this study, a permeable FW–H method was employed to explore the impact of the rotor-airframe interaction phenomenon on noise level. Furthermore, the impermeable surface method was utilized to examine the noise contributions of both the rotor and airframe, aiming to identify the dominant noise sources in the rotor-airframe configuration. Figure 21 presents the comparative results between the permeable and impermeable FW-H methods for the rotor-airframe configuration with $S/R = -0.1$. It can be observed that a noticeable difference was shown between the two approaches through the elevation angle from −30° to 30°, −150° to 150°. In particular, the largest discrepancy of 2.5 dB was observed at the in-plane location. The noise level results from the two approaches were similar, except for these specific locations, although it is the smallest distance between the rotor and airframe. Although the acoustic scattering by the airframe is included in the permeable surface simulation, the magnitude of OASPL and its directivity are similar to the results obtained from the impermeable surface method. It was concluded that the unsteady loading component arising from the interaction effects is the most dominant source of noise, rather than the influence of acoustic scattering and volume sources for the rotor-airframe configuration.

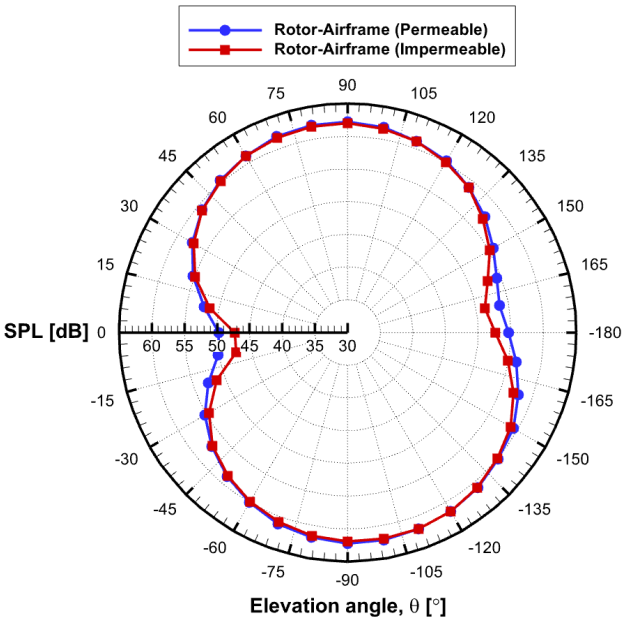

FIG. 21. OASPL directivity of rotor-airframe with $S/R = -0.1$ calculated by impermeable and permeable surface methods

Figure 22 shows the magnitudes of noise produced by the rotor and airframe calculated using the impermeable FW-H method. The purpose of this comparative analysis is to assess their respective contributions to the overall

noise level and identify the dominant noise source in the rotor-airframe configuration. Interestingly, the variation in airframe noise increased as the rotor-airframe separation distance decreased. The magnitude of airframe noise is comparable to the noise level generated by the rotor blade when the rotor blades are in closest proximity to the airframe. At specific microphone positions, the noise generated by the airframe was greater than that produced by the rotor and played a dominant role as the primary source of noise. As the distance between the airframe and rotor tip increased (*S/R*) from 0.1, 0.3, to 0.5, a significant reduction of 5–8 dB in noise was observed for all microphone positions. Notably, the noise reduction was more substantial from $S/R = -0.1$ to $S/R = -0.3$ than from $S/R = -0.3$ to $S/R = -0.5$. The airframe noise reduction is much more significant when compared to the reduction in rotor noise, primarily attributed to the effect of loading noise, as the airframe remains stationary. Therefore, thickness noise is not generated due to the stationary position of the airframe, and unsteady loading forces are periodically applied to the airframe by the rotation of the rotor. When the rotor blades rotate above the airframe, they create a strong wake flow that periodically induces aerodynamic loads on the airframe. To verify this, we compared the aerodynamic loads acting on the airframe in the x-, y-, and z-directions as a function of the rotor-to-airframe distance, as shown in Fig. 22. When the rotor-to-airframe distance was at its closest ($S/R = -0.1$), significant aerodynamic loads in the x-, y-, and z-directions were induced due to strong mutual interaction effects. It's worth mentioning that the force fluctuation along the y-axis results from the edgewise component of the wake flow, and the aerodynamic loads along the z-axis are due to the wake flow propagation. However, as the rotor-to-airframe distance increases and the mutual interaction effects diminish, the unsteady load components on the airframe due to the rotor wake become less prominent, resulting in a reduction in their contribution to airframe noise. Again, it is clear that the force fluctuation reduction is greater from $S/R = -0.1$ to $S/R = -0.3$ than from $S/R = -0.3$ to $S/R = -0.5$, as discussed in the context of noise reduction. It was concluded that the contribution of airframe noise becomes crucial and acts as the primary source of noise and it must be included in the overall noise level calculations as the gap between the rotor and airframe grew smaller.

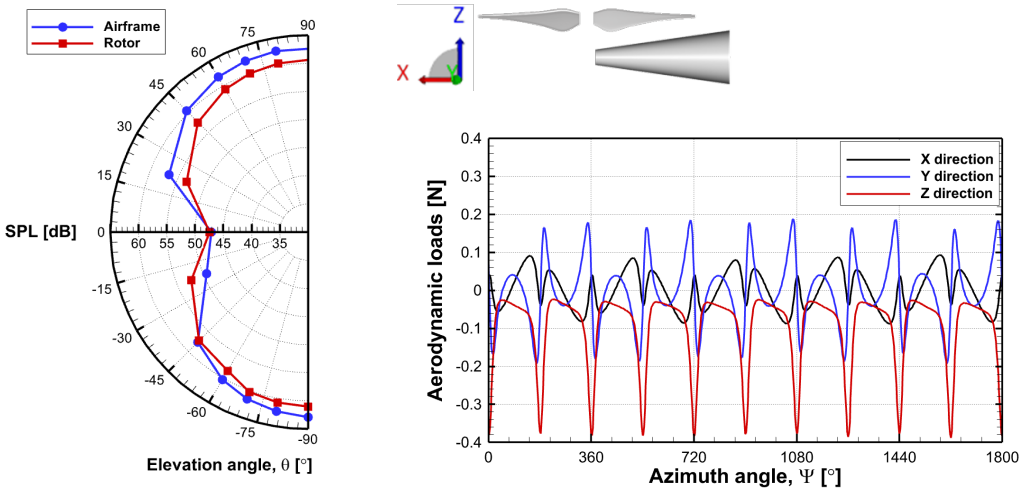

(a)

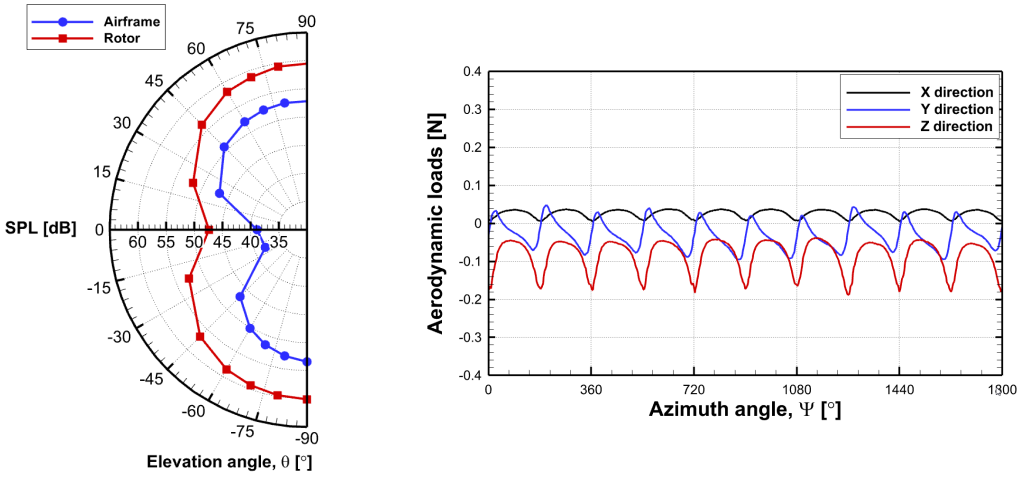

(b)

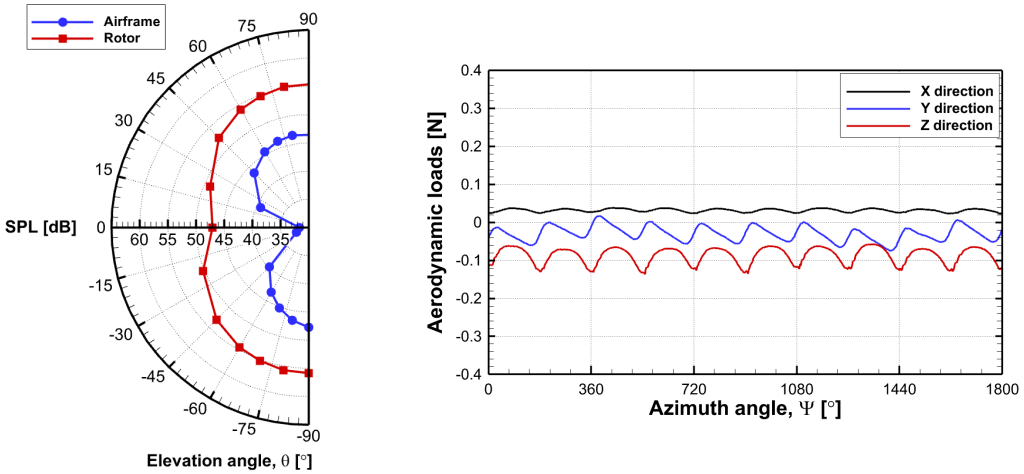

(c)

FIG. 22. Comparison of noise contributions (left) and time-history of force acting on the airframe (right) depending on the separations distance: (a) *S/R* = −0.1, (b) *S/R* = −0.3, (c) *S/R* = −0.5

4. CONCLUSIONS

In this study, a computational investigation was conducted to assess the impact of rotor-airframe interaction on aerodynamic and noise characteristics, considering different airframe shapes and varying distances between the rotor and airframe. Aerodynamic analysis was performed using an LBM simulation, and acoustic prediction was implemented using the FW-H acoustic analogy with a permeable surface. Prior to analyzing the changes in the flow field and noise characteristics owing to rotor-airframe interaction, the thrust levels for the rotation speed and directivity of the 1st and 2nd BPF at specific locations for an isolated rotor and tonal noise at BPFs for rotor-airframe cases were compared against experimental data. The validation results indicated that the LBM predictions were in excellent agreement with the experimental data, confirming the suitability of the LBM for research in aerodynamics and noise. Our findings about airframe shape effect, the rotor-airframe distance effect, and noise contribution are summarized as follows:

1. In the airframe shape effect results, the mean thrust level increased for the conical airframe case compared to the cylindrical airframe case, which was consistent with the static pressure on the blade surface. Additionally, when the conical airframe was present, the wake structure dissipated more rapidly after colliding with the airframe than in the presence of the cylindrical airframe.
2. Regarding the noise analysis, the highest harmonic amplitude was observed in the conical airframe case for microphone M1, located in the rotor in-plane area. This trend persisted for the first five BPF harmonics for microphones M3 and M5. However, after the first five BPFs, the cylindrical airframe resulted in higher harmonic amplitudes. Furthermore, the surface dB map indicated that the noise radiating from the airframe was influenced more by the wake interaction with the airframe than by the tip vortex.
3. In the rotor tip clearance effect results, significant thrust force fluctuations were observed at $S/R = -0.1$ due to the rotor-airframe interaction. However, thrust amplitudes decreased substantially with increasing distance. The evolution of wake structures, dependent on the separation distance, was discussed by examining vorticity contours, revealing the presence of a fountain flow at $S/R = -0.3$ and $S/R = -0.5$.
4. The SPL graph showed that after the 2nd BPF, the sound pressure level decreased with increasing distance between the airframe and rotor tip, regardless of the microphone location. There was a maximum noise level increase of 12 dB at $S/R = -0.1$ compared to the isolated rotor, which was comparable to the noise levels at $S/R = -0.3$.

5. Lastly, when the distance between the rotor and the airframe was the smallest, the noise levels originating from the rotor and airframe were comparable, with the airframe noise level even exceeding the rotor noise level at specific microphone positions. As the distance between the airframe and rotor tip increased, the reduction in airframe noise was more significant compared to the reduction in rotor noise. Increasing the rotor-airframe spacing effectively mitigated the aerodynamic loads acting on the airframe, leading to reduced airframe noise.

One limitation of the current study is that it exclusively focused on the hovering condition. In other words, when the vehicle is under forward-flight conditions, it is anticipated that the noise characteristics are likely to differ from those in the hover condition. Furthermore, the research will be expanded from a single rotor to a coaxial counter-rotating rotor, which is widely used in UAM and UAVs. Moreover, the effect of the initial phase difference on the aerodynamics and acoustics of a coaxial rotor with an airframe will be investigated in future studies. Lastly, the present paper has primarily focused on tonal noise, so predicting broadband noise will be discussed in our future study.

Acknowledgments

This study was supported by the National Research Foundation of Korea (NRF) grants funded by the Ministry of Science and ICT (grant numbers NRF-2017-R1A5A1015311 and NRF-2021R1C1C1010198). This research was supported by the regional innovation megaproject program through the Korea Innovation Foundation, funded by the Ministry of Science and ICT (Project Number: 2023-DD-UP-0026). This work was supported by the research grant of the Gyeongsang National University in 2022.

Declaration of competing interest

The authors have no conflicts to disclose.

References

[1] *eVTOL/Urban air mobility TAM update: A slow take-off, but sky's the limit*, Morgan Stanley (2021).

[2] *Study on the societal acceptance of urban air mobility in Europe*, European Union Aviation Safety Agency

(2021).

[3] A. J. Torija, Z. Li, and R. H. Self, “Effects of a hovering unmanned aerial vehicle on urban soundscapes perception,” Transp. Res. D 78 (2020).

[4] D. S. Little, J. Majdalani, R. J. Hartfield, Jr, and V. Ahuja, “On the prediction of noise generated by urban air mobility (UAM) vehicles. I. Integration of fundamental acoustic metrics,” Phys. Fluids 34(11), 116117 (2022).

[5] V. Ahuja, D. S. Little, J. Majdalani, and R. J. Hartfield, Jr, “On the prediction of noise generated by urban air mobility (UAM) vehicles. II. Implementation of the Farassat F1A formulation into a modern surface-vorticity panel solver,” Phys. Fluids 34(11), 116118 (2022).

[6] H. Lee and D. J. Lee, “Rotor interactional effects on aerodynamic and noise characteristics of a small multirotor unmanned aerial vehicle,” Phys. Fluids 32(4), 047107 (2020).

[7] W. Zhou, Z. Ning, H. Li, and H. Hu, “An experimental investigation on rotor-to-rotor interactions of small UAV propellers,” *35th AIAA Applied Aerodynamics Conference*, 3744 (2017).

[8] D. Shukla and N. Komerath, “Drone scale coaxial rotor aerodynamic interactions investigation,” J. Fluids Eng. 141(7), 071106 (2019).

[9] N. Intaratep, W. N. Alexander, W. J. Devenport, S. M. Grace, and A. Dropkin, “Experimental study of quadcopter acoustics and performance at static thrust conditions,” *Proceedings of 22nd AIAA/ CEAS Aeroacoustics Conferences*, (2016).

[10] S. B. Chae, S. C. Lee, and J. H. Kim, “Effects of rotor–rotor interaction on the wake characteristics of twin rotors in axial descent,” J. Fluid Mech. 952, A31 (2022).

[11] R. Piccinini, M. Tugnoli, and A. Zanotti, “Numerical investigation of the rotor-rotor aerodynamic interaction for eVTOL aircraft configurations,” Energies 13(22), 5995 (2020).

[12] Z. Jia and S. Lee, “High-fidelity computational analysis on the noise of a side-by-side hybrid VTOL aircraft,” J. Am. Helicopter Soc. 67(2), 1–14 (2022).

[13] Z. Jia and S. Lee, “Computational study on noise of urban air mobility quadrotor aircraft,” J. Am. Helicopter Soc. 67(1), 1–15 (2022).

[14] S. Li and S. Lee, “Prediction of urban air mobility multi-rotor VTOL broadband noise using UCD-QuietFly,” J. Am. Helicopter Soc. 66, 032004 (2021)

[15] N. S. Zawodny and D. D. Boyd Jr, “Investigation of rotor-airframe interaction noise associated with small-scale rotary-wing unmanned aircraft systems,” *American Helicopter Society 73rd Annual Forum.* (2017).

[16] C. D. Coffen, Tilt Rotor Hover Aeroacoustics*, NASA Contractor Report,* 177598 (1992).

[17] C. K. Rutledge, C. D. Coffen, and A. R. George, “A comparative analysis of XV-15 tiltrotor hover test data and WOPWOP predictions incorporating the fountain effect,” *NASA Contractor Report,* 189455 (1991).

[18] D. G. Caprace, A. Ning, P. Chatelain, and G. Winckelmans, “Effects of rotor-airframe interaction on the aeromechanics and wake of a quadcopter in forward flight,” Aerosp. Sci. Technol. 130 (2022).

[19] D. A. Wachspress, K. Y. Michael, K. S. Brentner, and Rotor, *airframe aeroacoustic prediction for EVTOL UAM aircraft*, *Vertical Flight Society's 75th Annual Forum and Technology Display*, (2019)

[20] Z. Wang, Q. Henricks, M. Zhuang, A. Pandey, M. Sutkowy, B. Harter, M. McCrink, J. Gregory, “Impact of rotor-airframe orientation on the aerodynamic and aeroacoustic characteristics of small unmanned aerial systems,” Drones 3(3), 56–73 (2019).

[21] L. A. J. Zori and R. G. Rajagopalan, “Navier-Stokes calculations of rotor-airframe interaction in forward flight,” J. Am. Helicopter Soc. 40(2), 57–67 (1995).

[22] Y. M. Park and S. Jee, “Numerical study on interactional aerodynamics of a quadcopter in hover with overset mesh in OpenFOAM,” Phys. Fluids 35(8), 085138 (2023).

[23] D. Casalino, W. C. P. Van der Velden, G. Romani, and I. Gonzalez-Martino, “Aeroacoustic analysis of urban air operations using the LB/VLES method,” *25th AIAA/CEAS Aeroacoustics Conference*. (2019).

[24] I. Gonzalez-Martino, G. Romani, J. Wang, and D. Casalino, “Rotor noise generation in a turbulent wake using lattice-Boltzmann methods*,” AIAA/CEAS Aeroacoustics Conference*, 3447 (2018).

[25] C. Thurman, J. Baeder, N. Zawodny, J. D. Baeder, “Computational prediction of broadband noise from a representative small unmanned aerial system rotor,” *76th Annual Forum & Technology Display*. (2020).

[26] S. Thibault, D. Holman, S. Garcia, and G. Trapani, G. “CFD Simulation of a quad-rotor UAV with rotors in motion explicitly modeled using an LBM approach with adaptive refinement,” *55th AIAA Aerospace Sciences Meeting*, 0583 (2017).

[27] S. Wen, J. Han, Z. Ning, Y. Lan, X. Yin, J. Zhang, and Y. Ge, “Numerical analysis and validation of spray distributions disturbed by quad-rotor drone wake at different flight speeds,” Comput. Electron. Agric. 166 (2019).

[28] W. C. P. Van der Velden, G. Romani, and D. Casalino, “Validation and insight of a full-scale S-76 helicopter rotor using the Lattice-Boltzmann Method,” Aerosp. Sci. Technol. 118 (2021).

[29] S. Chen and G. D. Doolen, “Lattice Boltzmann method for fluid flows,” Annu. Rev. Fluid Mech. 30(1), 329–364 (1998).

[30] Z. L. Yang, T. N. Dinh, R. R. Nourgaliev, and B. R. Sehgal, “Evaluation of the Darcy’s law performance for

two-fluid flow hydrodynamics in a particle debris bed using a lattice-Boltzmann model," Heat Mass Transf. 36(4), 295–304 (2000).

[31] M. E. Kutay, A. H. Aydilek, and E. Masad, "Laboratory validation of lattice Boltzmann method for modeling pore-scale flow in granular materials," Comput. Geotech. 33(8), 381–395 (2006).

[32] A. Zarri, E. Dell'Erba, W. Munters, and C. Schram, "Aeroacoustic installation effects in multi-rotorcraft: Numerical investigations of a small-size drone model," Aerosp. Sci. Technol. 128 (2022).

[33] G. Romani and D. Casalino, "Rotorcraft blade-vortex interaction noise prediction using the lattice-Boltzmann method," Aerosp. Sci. Technol. 88, 147–157 (2019).

[34] S. Shubham, *Computational Aeroacoustic Investigation of Co-rotating Rotors for Urban Air Mobility*, Delft University of Technology M.S. Thesis, (2020)

[35] N. Gourdain, R. Serré, T. Jardin, G. Delattre, and J. M. Moschetta, *Analysis of the flow produced by a low-Reynolds rotor optimized for low noise applications-Part 1: Aerodynamics*, (2017)

[36] R. B. Kotapati, R. Shock, and H. Chen, "Lattice-Boltzmann simulations of flows over backward-Facing inclined steps," Int. J. Mod. Phys. C 25(1), 1340021 (2014).

[37] H. Chen, S. Chen, and W. H. Matthaeus, "Recovery of the Navier-Stokes equations using a lattice-gas Boltzmann method," Phys. Rev. A 45(8), R5339–R5342 (1992).

[38] F. Avallone, W. C. P. Van Der Velden, D. Ragni, and D. Casalino, "Noise reduction mechanisms of sawtooth and combed-sawtooth trailing-edge serrations," J. Fluid Mech. 848, 560–591 (2018).

[39] N. S. Liu and T. H. Shih, "Turbulence modeling for very large-eddy simulation," A.I.A.A. J. 44(4), 687–697 (2006).

[40] C. Teruna, L. Rego, D. Casalino, D. Ragni, and F. Avallone, "A numerical study on aircraft noise mitigation using porous stator concepts," Aerospace 9(2), 70 (2022).

[41] Y. Li, Z. Ma, P. Zhou, S. Zhong, and X. Zhang, "A numerical investigation of the aerodynamic and aeroacoustic interactions between components of a multi-rotor vehicle for urban air mobility," J. Sound Vib. 571, 118002 (2024).

[42] P. V. Diaz and S. Yoon "High-fidelity computational aerodynamics of multi-rotor unmanned aerial vehicles," *2018 AIAA Aerospace Sciences Meeting*, 1266 (2018).

[43] N. S. Zawodny, D. D. Boyd, Jr, and C. L. Burley, "Acoustic characterization and prediction of representative, small-scale rotary-wing unmanned aircraft system components," *American Helicopter Society 72nd Annual Forum*. (2016).

[44] C. Nardari, D. Casalino, F. Polidoro, V. Coralic, P. T. Lew, and J. Brodie, “Numerical and experimental investigation of flow confinement effects on UAV rotor noise,” *25th AIAA/CEAS Aeroacoustics Conference*. 2497 (2019).

[45] W. S. Choi, Y. S. Choi, S. Y. Hong, J. H. Song, H. W. Kwon, and C. M. Jung, “Turbulence-induced noise of a submerged cylinder using a permeable FW-H method,” Int. J. Nav. Archit. Ocean Eng. 8(3), 235–242 (2016).

[46] Y. H. Yu, “Rotor blade–vortex interaction noise,” Prog. Aerosp. Sci. 36(2), 97–115 (2000).